Double pattern improves the Schlieren methods for measuring liquid-air interface topography

Jean Metzmacher[1*], Guillaume Lagubeau[1], Martin Poty[1] and Nicolas Vandewalle[1]

[1]GRASP, Institute of Physics, University of Liège, B5a, Liège, 4000, Belgium.

*Corresponding author(s). E-mail(s): jmetzmacher@uliege.be;

Abstract

The Schlieren method intends to reveal the elevation of a refractive fluid-fluid interface. The method is based on a comparison of images of a single pattern placed at the bottom of the container. Accurate measurements can be obtained with a simple and low cost optical setup. However, it is restricted to weak interface deformations, weak slopes and weak paraxial angles. To overcome these limitations, we propose an enhanced optical setup that uses a bitelecentric objective and a double pattern. Thanks to this new setup, we avoid geometrical approximations and we extend the method to moderate/large deformations. Moreover, the proposed method does not depend on the liquid depth and could be used in various applications.

1 Introduction

Measuring the topography of a fluid-fluid interface is of great importance in physics since it allows to observe and quantify elusive phenomena such as waves, instabilities or the presence of particles. For transparent fluids, this can be done with synthetic Schlieren methods (Sutherland et al, 1999; Dalziel et al, 2000; Raffel, 2015). Among them, the so-called Moisy-Rabaud-Salsac (MRS) method (Moisy et al, 2009) is an elegant method that gives accurate measurements with a simple and low cost optical setup. It can be reproduced in any laboratory and easily adapted for various applications. Despite its simplicity, Moisy et al (2009) reported a precision of 1 μm for a view field of 10 cm. This method has been successfully used in the case of Faraday waves (Eddi et al, 2011; Lau et al, 2020), wave-droplet interactions (Eddi et al, 2009; Damiano et al, 2016) and floating objects (Poty et al, 2014; Metzmacher et al, 2017; Vandewalle et al, 2020).

In the MRS method, a random points pattern is placed below (above) a container filled with a liquid and a camera, from above (below), takes pictures of the refracted pattern through the liquid. A comparison between pictures of the disturbed and undisturbed surface is done with a Digital Image Correlation (DIC) algorithm to compute the displacement field caused by the deformation of the interface. Then, geometric rules with some approximations are used to rely this displacement field to the surface gradient of the disturbed surface. Finally, the surface is reconstructed by integrating the gradient with a least-square method.

A key step is the computation of the displacement field between the pictures. DIC algorithms are well known and intensively used in lots of applications like Particle Image Velocimetry (Utami and Blackwelder, 1991; Meinhart et al, 1999; Adrian, 2005). However, they have some drawbacks (Meunier and Leweke, 2003; Bornert et al, 2009). They are rather slow and the

displacement is implicitly supposed constant at the window scale. To overcome some limitations of DIC algorithms, one can use algorithms based on recursive methods with multi-scale windows (Meinhardt-Llopis et al, 2013; Weinzaepfel et al, 2013) but these are complex and extremely time consuming.

Some alternatives and improvements have been proposed. Kolaas et al (2018) developed the Bichromatic Synthetic Schlieren method that computes the displacement field with two simultaneous images of a refracted pattern, taken with two different light wavelengths. Rajendran et al (2019) implemented a dot tracking algorithm. Spectral methods with checkerboard has also been proposed to replace DIC algorithms (Wildeman, 2018b; Grédiac et al, 2020). Among them, Wildeman (2018b) proposed a method based on Fourier demodulation, called Fast Checkerboard Demodulation (FCD) method. Instead of a random pattern, he uses a 2D checkered pattern with a high spatial frequency. In the spatial Fourier domain, the disturbed interface results in a deformation signal that modulates the high frequency signal of the pattern and classic Fourier demodulation techniques can be used to extract this deformation signal. This method is much faster than DIC algorithms and offers some other benefits: the displacement field is computed at each pixel of the image and the level of noise is lower (Wildeman, 2018b).

However, even if the displacement field is perfectly known, the MRS method suffers from the following main limitations (Moisy et al, 2009):

1. As the interface is reconstructed by integrating the surface gradient, uniform changes in the interface height are not detected.
2. For strong curvatures or large surface-pattern distances, caustics appear and it is no longer possible to compute properly the displacement field.
3. Slight vibrations of the setup can add noise components to the displacement field.
4. Since calculations are linearized, the method is limited to weak deformations, weak slopes and weak paraxial angles.

The two first limitations are intrinsic to the background Schlieren method and the third one can be prevented with a stable optical setup. The last and most restrictive one is mainly caused by the geometrical approximations used to rely the displacement field to the surface gradient. In the calculations, only first order terms are considered and the local liquid depth of the deformed interface is supposed equal to the liquid depth of the undisturbed interface. Moreover, errors on the measurement of the liquid depth can impact drastically the surface gradient estimation.

In this paper, we propose to improve the Schlieren method in order to reach moderate and large deformations/slopes. Moreover, this improved method does not depend on the liquid depth and can be used in various applications in which the liquid depth varies or is difficult to measure like spreading drops. However, rays crossings and caustics still prevent proper measurements of strong curvatures.

2 Method

In this section, let us consider the original method and a step-by-step description of additional improvements.

2.1 Moisy-Rabaud-Salsac method

The MRS method is based on the standard synthetic Schlieren method used for density varying fluids (Moisy et al, 2009). As illustrated on Fig. 1, a light source illuminates a pattern placed below a container filled with a liquid. Above the container, a camera takes pictures of the refracted pattern trough the interface. A DIC algorithm is used to compare the pictures of both disturbed and undisturbed surfaces and to compute the displacement field.

The next step is to establish a relationship between the displacement field and the surface gradient. As illustrated on Fig. 2, the geometry of the light rays is quite complex. The incidence plane, which is defined as the plane CPP' containing the camera C, the point P and its image P', is inclined and does not contain the optical axis. So, the displacement PP' does not take place along the radial direction with respect to the optical axis but in a direction $\hat{s}$, which corresponds to the intersection of the horizontal plane and the incidence plane CPP'. Because of that, Moisy et al (2009) used three approximations to compute the surface gradient from the displacement field. These approximations limit the method to

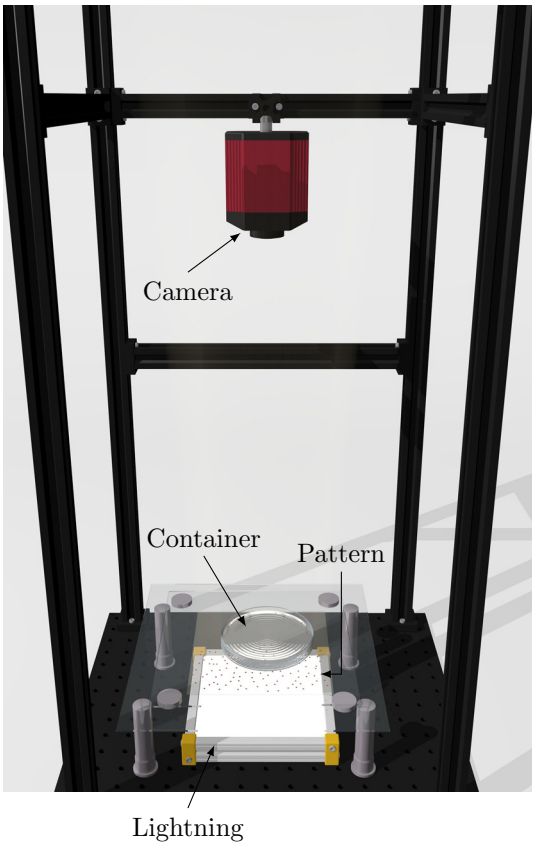

Fig. 1 Illustration of an MRS experimental setup. A light source illuminates from below a random points pattern. Above it, a container filled with a transparent liquid is placed on a glass plate. A camera takes pictures of the surface of the liquid from above

weak slopes, weak deformations and weak paraxial angles, and are the following:

1. *Paraxial approximation.* To be satisfied, the distance between the pattern and the camera must be much larger than the distance h_p between the pattern and the interface.
2. *Weak slope.* This implies that the surface slope θ and the incident angle i are weak ($\sin(i) \approx \tan(i) \approx i$ and $\cos(i) \approx 1$). So, only first order terms in i and θ are considered in the computations.
3. *Weak amplitude.* This implies that the local height of the liquid h_l is supposed to be equal to the mean height of the undisturbed surface h_0.

Considering theses approximations, it can be shown that the gradient field can be computed from the displacement field with a linear relationship

$$\vec{\nabla} h = -\frac{\delta \vec{r}}{h^*}, \quad \text{with} \quad \frac{1}{\mathrm{h}^*} = \frac{1}{\alpha \mathrm{h_s}} - \frac{1}{\mathrm{H}} \qquad (1)$$

where $\alpha = 1 - \frac{n_a}{n_l}$, $h_s = h_0 + h_c \frac{n_l}{n_c} + h_a \frac{n_l}{n_a}$ is an effective distance between the pattern and the surface of the liquid and H is the distance from the camera to the pattern. The last step is to integrate the surface gradient to reconstruct the interface. This is done with a least-square algorithm.

2.2 Fast Checkerboard Demodulation

The FCD method proposed by Wildeman (2018b) is a variation of the MRS method. Both methods share the same optical setup and geometrical approximations. They differ only on the computation of the displacement field. The FCD method uses a 2D checkered pattern and fast Fourier demodulation, instead of a random points pattern and a DIC algorithm.

In the FCD method, the spatial signal of the checkered pattern behaves like a carrier, as in frequency modulation of airwaves. This carrier is extracted from the picture of the undisturbed (flat) interface. On the picture of the disturbed interface, a deformation signal phase modulates the carrier signal. Usual Fourier demodulation techniques are used to recover the deformation signal from the phase modulated signal. Then the displacement field is obtained by transforming back the deformation signal in the spatial domain.

2.3 Bitelecentric objective

A first step to improve the original setup of the MRS method is to place a bitelecentric objective with a high aperture on the camera. With this objective, only vertical rays (rays parallel to the optical axis) coming from the pattern reach the camera. This allows to avoid parallax effects and to greatly simplify the optical ray tracing and calculations.

As only vertical rays reach the camera, the incident plan, defined as the plane containing the camera C, the point P and its image P', contains

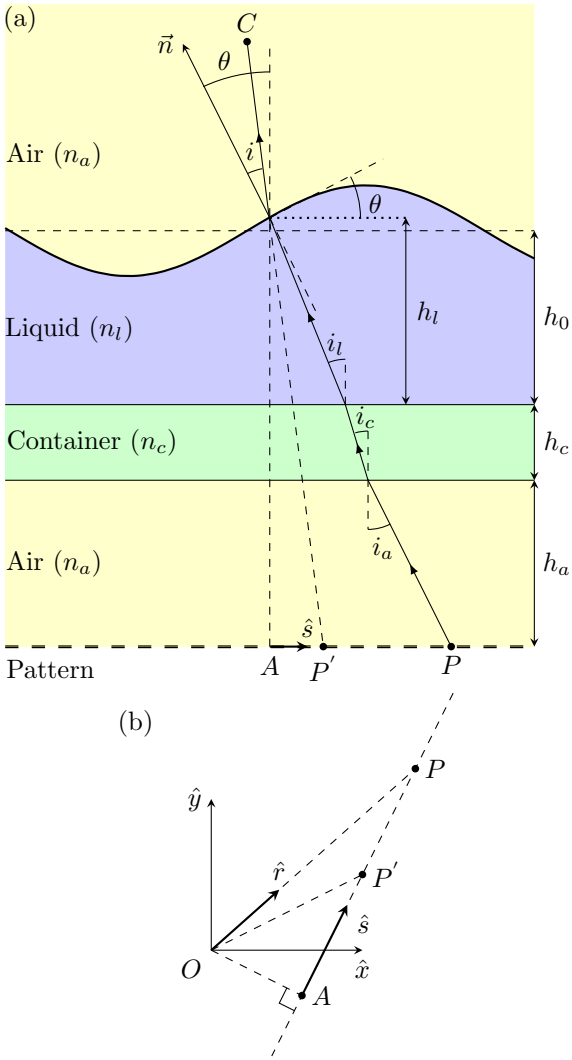

Fig. 2 In the original MRS method, an inclined optical ray coming from the pattern point P appears to come from the image $P^{'}$. The incidence plane $CPP^{'}$ does not contain the optical axis and so, is inclined. (a) Inclined incidence plane $CPP^{'}$. (b) Positions of the point P and its image $P^{'}$ on the xy plane (pattern plane). The direction $\hat{s}$ corresponds to the intersection of the xy plane and the incidence plane

the optical axis and is vertical (Fig. 3). So, the gradient is equal to the slope of the curve in direction $\hat{r}$ and we get the following relationship

$$\vec{\nabla} h = \tan(i)\hat{r} \tag{2}$$

between the gradient field and the incident angle i without any approximation.

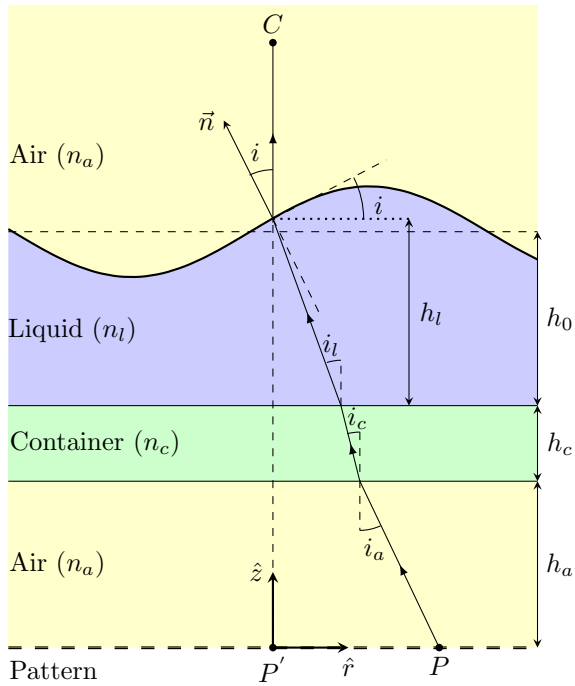

Fig. 3 Incidence plane obtained with a bitelecentric objective. As only vertical refracted rays reach the camera, the image $P^{'}$ of point P is located at the intersection of the optical axis and the pattern. Therefore, the incidence plane $CPP^{'}$ is vertical

2.4 Double pattern

A second improvement is the use of a double pattern. Each pattern is placed at a specific height, as illustrated in Fig. 4. The distance h_p between the patterns can be fixed and accurately known. In this setup, the camera has to take four images instead of two: (i) pattern 1 through the undisturbed interface, (ii) pattern 2 through the undisturbed interface, (iii) pattern 1 through the disturbed interface and (iv) pattern 2 through the disturbed interface.

By comparing both images of pattern 1, the displacement $PP^{'}$ between a point P of the pattern 1 and its image $P^{'}$ trough the deformed surface can be computed by a DIC algorithm or by Fourier demodulation (if a checkered pattern is used). The displacement $QQ^{'}$ between a point Q of the pattern 2 and its image $Q^{'}$ trough the deformed surface can be computed exactly the same way. The distance h_p between the patterns being known, the angle i_a can be computed from these

two displacements by

$$i_a = \arctan\left(\frac{\delta r}{h_p}\right) \tag{3}$$

where $\vec{\delta r} = \vec{PP'} - \vec{QQ'}$. Applying the Snell-Descartes law at each interface, we get a relationship between the incidence angle i and the angle i_a:

$$i_a = \arcsin\left\{\frac{n_l}{n_a}\sin\left[i - \arcsin\left(\frac{n_a}{n_l}\sin(i)\right)\right]\right\} \tag{4}$$

This relationship cannot be inverted but, numerically, we can use i_a obtained from Eq. (3) to interpolate the function and evaluate i. Once we get the incidence angle i, the gradient can be computed with Eq. (2). However, this gives only the magnitude of the gradient. Its orientation ϕ can be determined with the components of the displacement field by

$$\phi = \arctan\left(\frac{\delta r_y}{\delta r_x}\right) \tag{5}$$

Knowing the magnitude and the orientation of the gradient, one can compute its x and y components and integrate them to reconstruct the surface slope.

With the double pattern, one avoids any geometrical approximations and calculations become independent of the liquid depth. The only height implied in the calculations is the distance between the patterns. All the intermediate layers between the top screen and the interface, as the container wall, do not appear in Eq. (4). Thanks to these improvements, moderate to large deformations can be measured. The method can be used in new applications in which the depth of the undisturbed liquid is not constant. Nevertheless, it is still limited to moderate slopes because strong slopes may cause ray crossings, resulting in multiple images of the same point. The main drawback is that the imaged area is limited by the bitelecentric objective. This method is also more time consuming as four images and two displacement fields should be taken into account. However, it is possible to take pictures of two color patterns at the same time as we explain in sect. 3 and the Fast Checkeredboard Demodulation technique allows fast computations of the displacement fields.

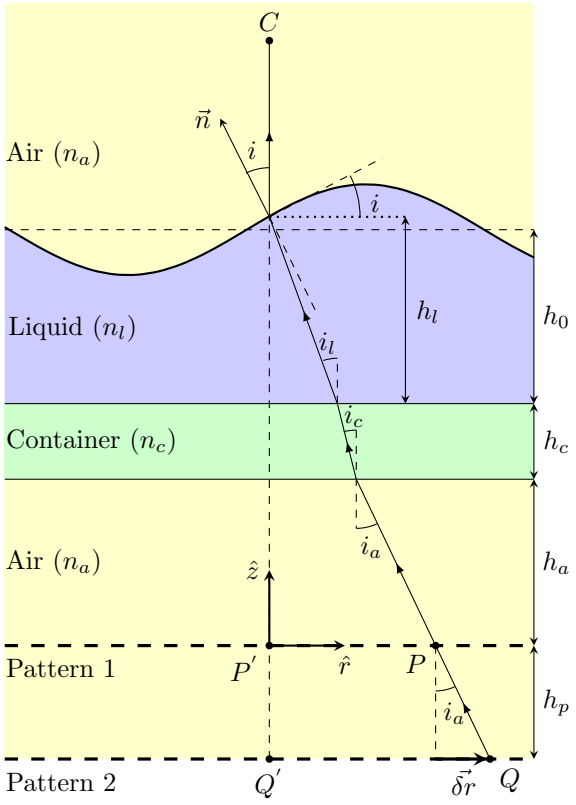

Fig. 4 Optical rays geometry when a second pattern at a different height under the container is used. A second displacement QQ' can be computed. Knowing the difference of height h_p between the patterns, the angle i_a can be computed from δr, the difference of both displacements PP' and QQ'. A relationship can be established between i_a and the incidence angle i by applying the Snell-Descartes law at each interface. This relationship does not depend on the liquid height

3 Setup and computations

A 2448 × 2048 color camera with a bitelecentric objective with a 118.06 mm × 98.47 mm field of view is placed above a glass plate. Two color patterns, one red and one blue, are generated numerically with the Matlab scripts written by Wildeman (2018a) and made available on GitHub. The patterns are printed on 4 mm thick glass plates and placed at different heights below the container. The blue pattern is on the bottom face of the top (blue edge) glass plate and the red pattern is on the top face of the bottom (red edge)

glass plate in order to only have an air layer between them as shown in Fig. 5. These two glass plates are separated by spacers of accurate height.

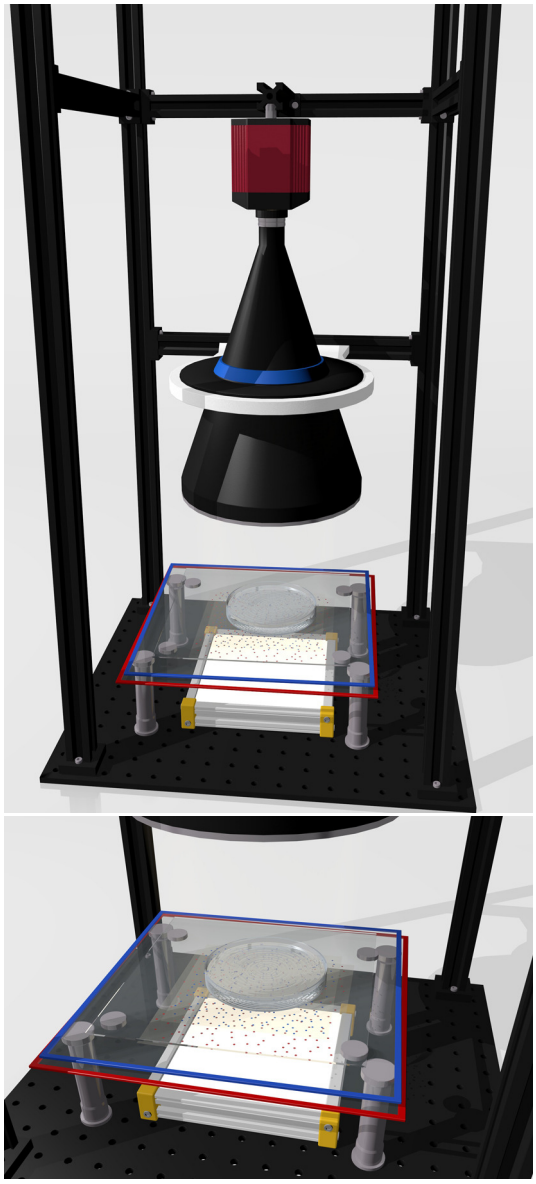

Fig. 5 Illustration of the proposed experimental setup. A camera with a bitelecentric objective is placed above a container and a double pattern. Each pattern is printed on a glass plate and placed at a specific height below the container. The blue one is on the bottom face of the blue edge glass plate and the red one is on the top face of the red edge glass plate. As there is only an air layer of constant thickness between the patterns, the surface gradient can be computed with Eqs. (2)-(4) and then integrated. Top: view of the entire setup. Bottom: zoom on the double pattern

Pictures of the patterns through the undisturbed and the disturbed surfaces are taken. The R and B channels are extracted from these color images and binarized by thresholding in order to separate each pattern. The red pattern appears black on blue channel and blue pattern appears black on red channel.

The displacement field of each pattern and the angle i_a are then computed. A cubic spline interpolation is used to get the angle i from i_a with Eq. (4). The surface gradient is easily obtained from Eq. (2) and then integrated to get the height of the interface. The calculations of the displacement fields and the integration of the surface gradient are performed with the Matlab script written by Wildeman (2018a).

The measurements are done with two type of patterns, random points patterns (in sect. 4.1) and checkerboards (in sect. 4.2). Fig. 6 shows images of these patterns taken by the camera. The random points pattern is used with a DIC algorithm. The size of the dots is 0.2 mm and the density is 0.26. The blue checkerboard is used with the FCD algorithm and the side of the squares is 0.5 mm long.

4 Results

Two typical applications are presented in order to emphasize the advantages of the present method.

4.1 Slope measurements

In order to validate our improvements, we have applied the method to glass wedges with specific angles and compared the wedge angles to the measured slopes, as shown in Fig. 7. The glass wedges are circular and have a diameter of 25.4 mm. Their angle ranges from 2° to 25°. In order to avoid errors caused by the sharp borders of the wedges, pictures taken by the camera are cut and the measurements are only done on square windows inscribed in the circular wedges. As all the points of the deformed image are displaced, random points patterns are used and the displacement fields are computed by the DIC algorithm written by Wildeman (2018a). The FCD method is not adapted in this case because the displacement of all points can be bigger than the checkerboard wavelength. Five measurements are done for each wedge with random orientations. The mean angles

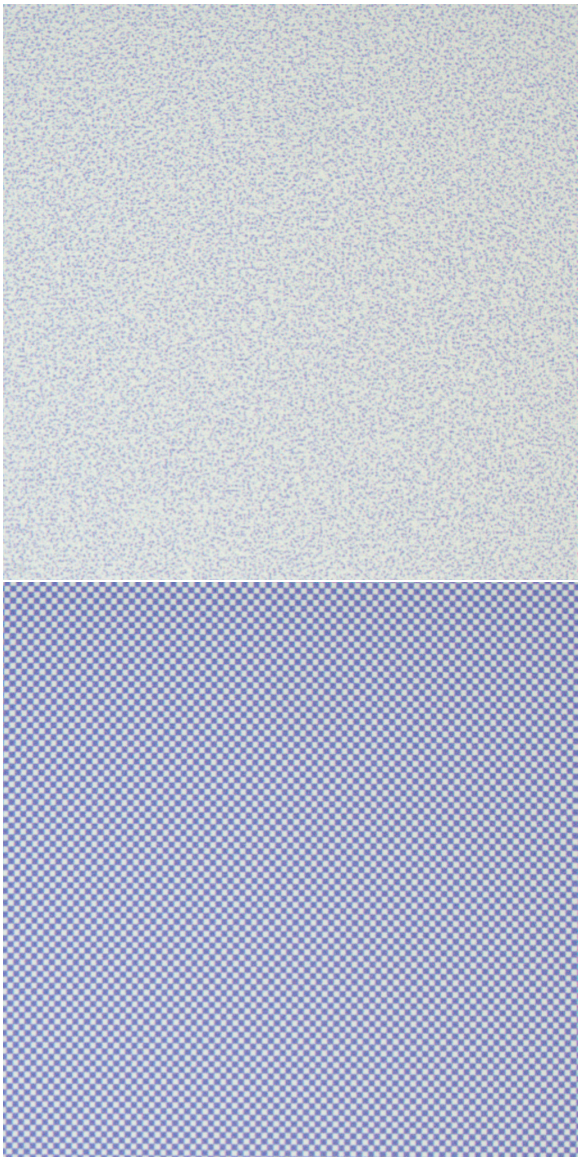

Fig. 6 Images of the blue patterns used to compute the displacement fields. These images are taken by the camera with a region of interest of 1024 x 1024 pixels. Top: blue random points pattern used with DIC algorithm. The size of the dots is 0.2 mm and the density is 0.26. Bottom: blue checkerboard used with the FCD algorithm. The side of the squares is 0.5 mm long

measured for each wedge are shown on Fig. 7. One can see that the proposed method performs better than the MRS method when the slopes increases. Indeed, we measured angles up to 25° with an excellent accuracy whereas the MRS method becomes inaccurate for the largest angles. This is because Moisy et al (2009) consider only first order terms in computations.

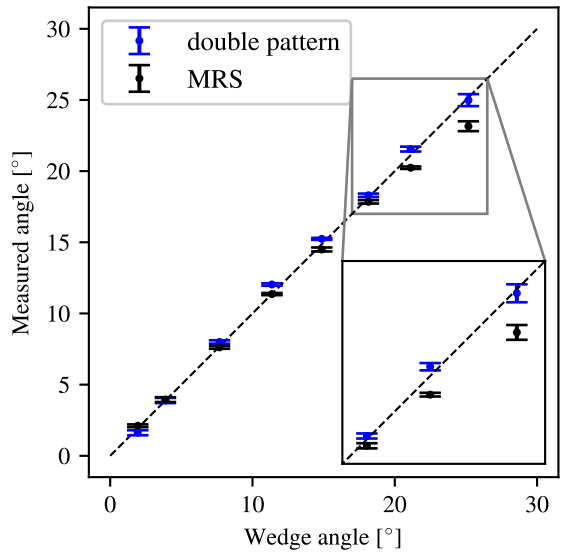

Fig. 7 Mean angle of wedges measured by our method as a function of the true angle value. Slopes up to 25° have been measured with an excellent accuracy. The displacement fields are computed by the DIC algorithm written by Wildeman (2018a)

The other main limitation of the MRS method is the weak amplitude approximation, which is masked when one consider only the mean angle of a wedge. Because of this approximation, the MRS method underestimates (overestimates) the slope when the local height is lower (greater) than the mean height. By computing the mean angle on a symmetric area around the center of the wedge, underestimations and overestimations cancel. To illustrate the limitation of the weak amplitude approximation, the local measured angle of a 18.15° degrees wedge with both methods is shown on Figs. 8 and 9. The orientation of the wedge is -36.13° degrees from the x axis. Although the mean value of the slope is close to the true one (as it can be seen on Fig. 7), Figs. 8 and 9 shows that the MRS method fails to recover the correct angle along the wedge. The value is overestimated or underestimated, except at the center. With our method, a constant angle is obtained as expected.

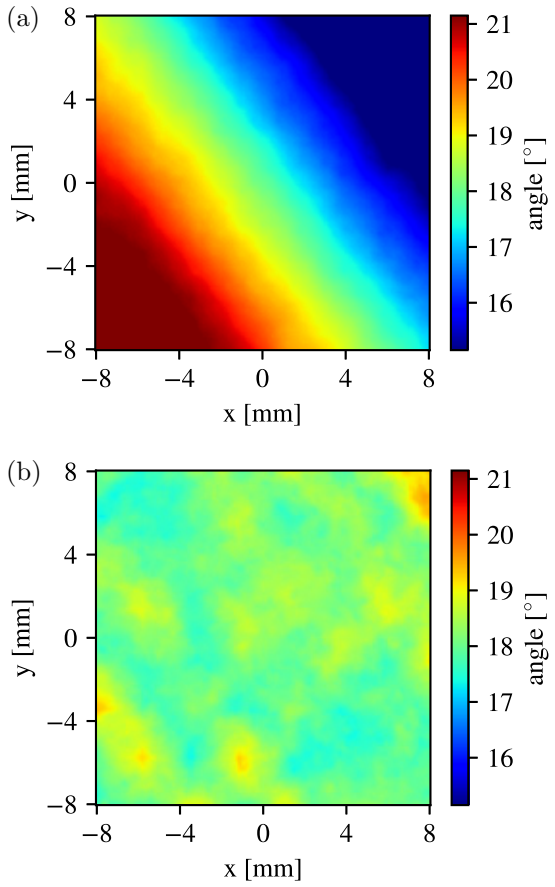

Fig. 8 Local measured angle of a 18.15° wedge. The orientation of the wedge is -36.13° from the x axis. (a) MRS method. (b) Proposed method. The displacement fields are computed by the DIC algorithm written by Wildeman (2018a)

4.2 Floating object

For simple floating objects the theoretical profile of the liquid can be computed (Chan et al, 1981; Kralchevsky and Denkov, 2001; Vella and Mahadevan, 2005; Poty and Vandewalle, 2021). Especially, the liquid deformation h around a spherical particle should behave like a Bessel function of the second kind K_0 centered on the particle (Kralchevsky and Denkov, 2001; Vella and Mahadevan, 2005)

$$h = QK_0(r/\lambda), \quad \text{with} \quad \mathrm{Q} = \mathrm{r_c} \sin\psi \qquad (6)$$

where Q is the capillary charge being a constant that characterizes the depth of the deformation

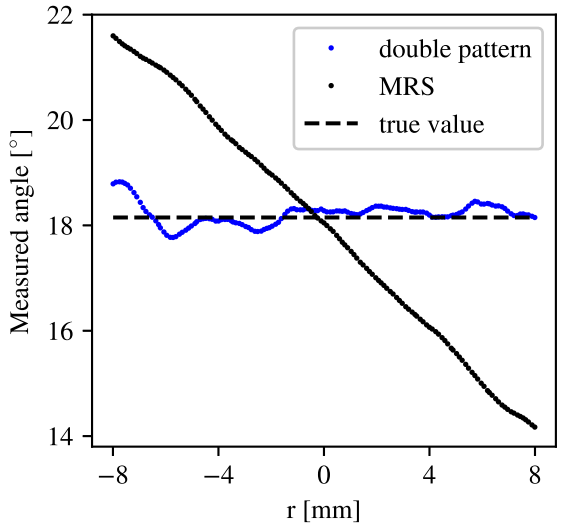

Fig. 9 Profile of the measured angle along the wedge orientation. The slope of the wedge is 18.15° and its orientation is -36.13° from the x axis. r is the distance from the center. The displacement fields are computed by the DIC algorithm written by Wildeman (2018a)

around the object, r is the distance from the center of the particle, λ is the capillary length being $\lambda \approx 2.7\,\mathrm{mm}$ for water-air interfaces, r_c is the radius of the contact line and ψ is the slope angle at the contact line. This expression allows for measuring profiles but also capillary charges. A sketch of the typical deformation around a heavy sphere is shown in Fig. 10.

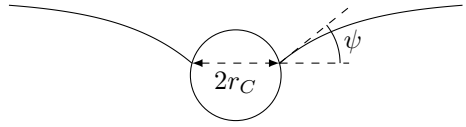

Fig. 10 Sketch of the surface deformation around a floating sphere. The density of the sphere is greater than the density of the liquid. The depth of deformation around the particle can be characterizes by a capillary charge $Q = r_c \sin\psi$ where r_c is the radius of the contact line and ψ is the slope angle at the contact line

In the MRS method, the displacement field depends on the liquid height as one can see on Fig. 2. To reconstruct the interface, Moisy et al (2009) established a relationship (see Eq. (1)) between the displacement field and the surface gradient that implies the mean liquid height. If the liquid height is not measured accurately or changes during the experiments, it will cause (large) errors on the reconstructed interface. In the case

of a floating sphere, it will impact the capillary charge Q.

In the present method, the surface gradient can be computed exactly with Eqs. (2)-(4), and these computations do not imply the liquid height. In order to check that the reconstructed interface is really independent of the liquid height, we measured the deformations around a 3 mm radius sphere floating in water baths of different depths and we fitted the experimental data with Eq. (6). Fig. 11 shows the mean profile around the sphere in water baths of 10.84 mm and 7.04 mm deep. Our data overlap and are in good agreement with the theoretical profile and the capillary charges obtained by fitting the data are similar (see Table 4.2). So, the presented method recovers well the same profile (and thus the same capillary charge) in both water baths without measuring the liquid height. The displacement fields on the top pattern are illustrated on Fig. 12 for the 7.04 mm deep bath. Similar displacement fields are obtained on the bottom pattern. Fig. 13 shows the reconstructed surface.

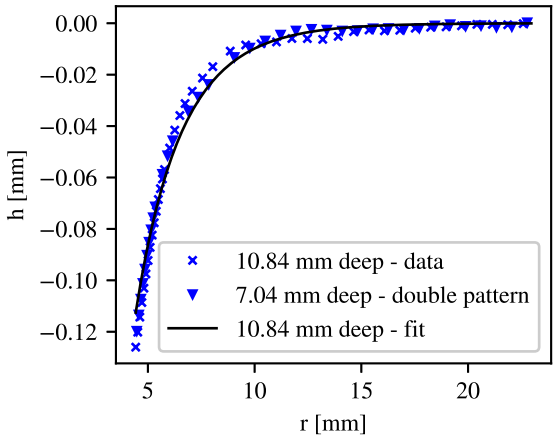

Fig. 11 Mean profile of the surface around a 3 mm radius sphere floating in water as a function of the distance r from its center. The measurements were done with water baths of 10.84 mm and 7.04 mm deep. The data overlap and are in good agreement with the theoretical profile (Eq. (6)). The displacement fields were computed with the FCD algorithm written by Wildeman (2018a)

We also compare our measurements with the MRS method. Fig. 14 shows the mean reconstructed profile of the surface around the 3 mm radius sphere floating in a water bath of 7.04

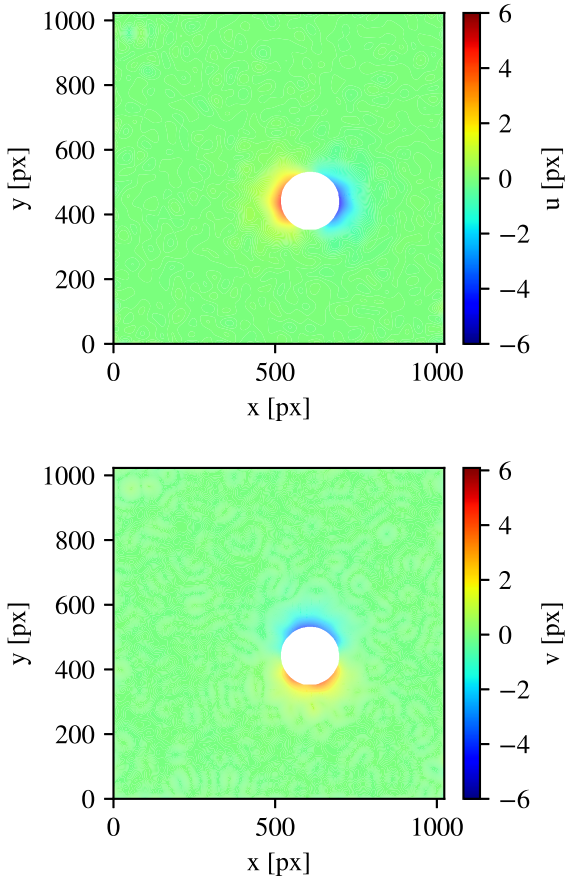

Fig. 12 Measured displacement fields on the top pattern for 3 mm radius sphere floating in water. Similar displacement fields are obtained for the bottom pattern. The water bath is 7.04 mm deep. Top: displacement field u along the x direction. Bottom: displacement field v along the y direction. The displacement fields were computed with the FCD algorithm written by Wildeman (2018a)

mm depth with both methods. The profile recovers with the MRS method is similar to the one obtained with the proposed method. However, the capillary charges computed by fitting the data are a bit larger (in absolute value) as we can see in Table 4.2. If the mean liquid height is not perfectly measured, the reconstructed profile obtained by the MRS method will be affected. Table 4.2 shows the impact on the measured capillary charge if the mean liquid height is underestimated by 5% and 10% when the water bath is 7.04 mm deep. As expected given Eq. (1), the charge is overestimated (in absolute value). The error on the capillary charge is not so important in this case because a 4 mm thick glass plate is placed between the pattern

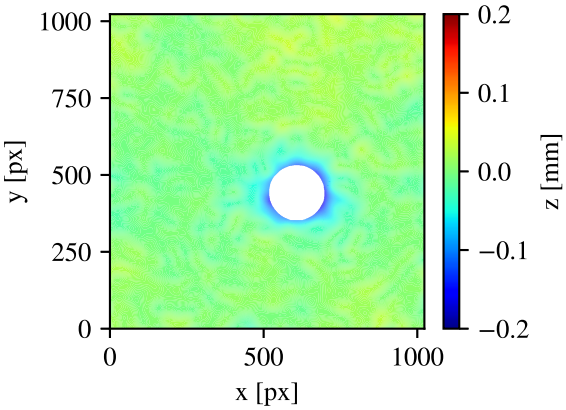

Fig. 13 Reconstructed surface around a 3 mm radius sphere floating in water bath of 7.04 mm deep with the proposed method. The displacement fields were computed with the FCD algorithm written by Wildeman (2018a)

and the container. This attenuates the change in the effective distance h_s that appears in Eq. (1). The displacement fields were computed with the FCD algorithm written by Wildeman (2018a).

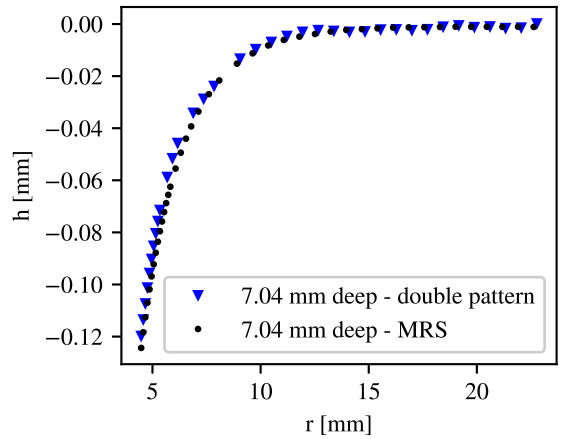

Fig. 14 Mean profile of the surface around a 3 mm radius sphere floating in water as a function of the distance r from its center. The measurements were done in a water bath of 7.04 mm deep with MRS method and the proposed method. The displacement fields were computed with the FCD algorithm written by Wildeman (2018a)

5 Conclusion

The Moisy-Rabaud-Salsac (MRS) method is a synthetic Schlieren method widely used to measure the topography of refractive interfaces. It requires only a simple and low cost optical setup, and can be easily reproduced in any laboratory. However, it is limited to weak amplitudes, weak slopes and weak paraxial angles. Based on the MRS method, this paper presents a new method that uses a bitelecentric objective and a double pattern. Thanks to this enhanced but still simple optical setup, geometrical approximations are avoided and moderate slopes and deformations can be measured. However, (very) strong curvatures still cannot be measured because of ray crossings.

The use of a bitelecentric objective simplifies greatly the geometry of the light rays. A relationship between the gradient field and the incident angle can be immediately obtained without approximations.

A double pattern, composed of two patterns at specific heights, allows to compute the incidence angle without approximations and without measuring the height of the transparent medium. This improvement opens the way to new applications in which the liquid height varies or cannot be easily measured. We demonstrated in two different experimental situations the advantages of the proposed method.

Water height [mm]	Capillary charge [mm]	Method
10.84	-0.631	2 patterns
7.04	-0.623	2 patterns
10.84	-0.683	MRS
7.04	-0.679	MRS
7.04 - 5%	-0.719	MRS
7.04 - 10%	-0.743	MRS

Table 1 Capillary charges measured by fitting the surface profile around a 3 mm radius sphere floating in water. Both methods are used with water baths of different depth. In the case of the MRS method, the impact on the measured capillary charge is shown when the mean liquid height is underestimated by 5% and 10% for a water bath of 7.04 mm deep. The displacement fields were computed with the FCD algorithm written by Wildeman (2018a)

Authors' contributions

J. Metzmacher, G. Lagubeau and M. Poty contributed to the conception of the proposed method. J. Metzmacher, M. Poty and N. Vandewalle wrote the manuscript.

Acknowledgments. We thank Y. E. Corbisier for his support to draw 3d sketches and pictures for this paper.

Statements and Declarations

Funding

This work is financially supported by the University of Liège through the CESAM Research Unit.

Conflict of interest

The authors have no competing interests to declare that are relevant to the content of this article.

References

Adrian RJ (2005) Twenty years of particle image velocimetry. Exp Fluids 39:159. https://doi.org/10.1007/s00348-005-0991-7

Bornert M, Brémand F, Doumalin P, et al (2009) Assessment of Digital Image Correlation Measurement Errors: Methodology and Results. Exp Mech 49:353. https://doi.org/10.1007/s11340-008-9204-7

Chan DYC, Henry, JD Jr, White LR (1981) The interaction of colloidal particles collected at fluid interfaces. J Colloid Interface Sci 79(2):410. https://doi.org/10.1016/0021-9797(81)90092-8

Dalziel SB, Hugues GO, Sutherland BR (2000) Whole-field density measurements by 'synthetic schlieren'. Exp Fluids 28:322. https://doi.org/10.1007/s003480050391

Damiano AP, Brun PT, Harris DM, et al (2016) Surface topography measurements of the bouncing droplet experiment. Exp Fluids 57:163. https://doi.org/10.1007/s00348-016-2251-4

Eddi A, Fort E, Moisy F, et al (2009) Unpredictable Tunneling of a Classical Wave-Particle Association. Phys Rev Lett 102:240,401. https://doi.org/10.1103/PhysRevLett.102.240401

Eddi A, Sultan E, Moukhtar J, et al (2011) Information stored in Faraday waves: the origin of a path memory. J Fluid Mech 674:433. https://doi.org/10.1017/S0022112011000176

Grédiac M, Blaysat B, Sur F (2020) Comparing several spectral methods used to extract displacement fields from checkerboard images. Opt Lasers Eng 127:105,984. https://doi.org/10.1016/j.optlaseng.2019.105984

Kolaas J, Riise BH, Sveen K, et al (2018) Bichromatic synthetic schlieren applied to surface wave measurements. Exp Fluids 59:128. https://doi.org/10.1007/s00348-018-2580-6

Kralchevsky PA, Denkov ND (2001) Capillary forces and structuring in layers of colloid particles. Curr Opin Colloid Interface Sci 6(4):383. https://doi.org/10.1016/S1359-0294(01)00105-4

Lau YM, Westerweel J, van de Water W (2020) Using Faraday Waves to Measure Interfacial Tension. Langmuir 36(21):5872. https://doi.org/10.1021/acs.langmuir.0c00622

Meinhardt-Llopis E, Sánchez J, Kondermann D (2013) Horn-schunck optical flow with a multi-scale strategy. Image Proc On Line 3:151. https://doi.org/10.5201/ipol.2013.20

Meinhart CD, Wereley ST, Santiago JG (1999) PIV measurements of a microchannel flow. Exp Fluids 27:414. https://doi.org/10.1007/s003480050366

Metzmacher J, Poty M, Lumay G, et al (2017) Self-assembly of smart mesoscopic objects. Eur Phys J E 40:108. https://doi.org/10.1140/epje/i2017-11599-y

Meunier P, Leweke T (2003) Analysis and treatment of errors due to high velocity gradients in particle image velocimetry. Exp Fluids 35:408. https://doi.org/10.1007/s00348-003-0673-2

Moisy F, Rabaud M, Salsac K (2009) A synthetic Schlieren method for the measurement of the topography of a liquid interface. Exp Fluids 46:1021. https://doi.org/10.1007/s00348-008-0608-z

Poty M, Vandewalle N (2021) Equilibrium distances for the capillary interaction between floating objects. Soft Matter 17:6718. https://doi.org/10.1039/D1SM00447F

Poty M, Lumay G, Vandewalle N (2014) Customizing mesoscale self-assembly with three-dimensional printing. New J Phys 16(2):023,013. https://doi.org/10.1088/1367-2630/16/2/023013

Raffel M (2015) Background-oriented schlieren (BOS) techniques. Exp Fluids 56:60. https://doi.org/10.1007/s00348-015-1927-5

Rajendran LK, Bane SPM, Vlachos PP (2019) Dot tracking methodology for background-oriented schlieren (BOS). Exp Fluids 60:162. https://doi.org/10.1007/s00348-019-2793-3

Sutherland BR, Dalziel SB, Hugues GO, et al (1999) Visualization and measurement of internal waves by synthetic schlieren. Part 1. Vertically oscillating cylinder. J Fluid Mech 390:93. https://doi.org/10.1017/S0022112099005017

Utami T, Blackwelder RE (1991) A cross-correlation technique for velocity field extraction from particulate visualization. Exp Fluids 10:213. https://doi.org/10.1007/BF00190391

Vandewalle N, Poty M, Vanesse N, et al (2020) Switchable self-assembled capillary structures. Soft Matter 16:10,320. https://doi.org/10.1039/D0SM01251C

Vella D, Mahadevan L (2005) The "Cheerios effect". Am J Phys 73:817. https://doi.org/10.1119/1.1898523

Weinzaepfel P, Revaud J, Harchaoui Z, et al (2013) DeepFlow: Large Displacement Optical Flow with Deep Matching. In: Proceedings of the IEEE International Conference on Computer Vision (ICCV), p 1385

Wildeman S (2018a) Matlab implementations of fcd and dic+of methods. https://github.com/swildeman/fcd, https://github.com/swildeman/dicflow

Wildeman S (2018b) Real-time quantitative Schlieren imaging by fast Fourier demodulation of a checkered backdrop. Exp Fluids 59:97. https://doi.org/10.1007/s00348-018-2553-9